

Pulmonary Delivery of Engineered Exosomes to Suppress Postoperative Melanoma Lung Metastasis through Preventing Premetastatic Niche Formation

Xiaoqing Han

Changchun Institute of Applied Chemistry, Chinese Academy of Sciences

Luopeng Bi

Department of Urology, First Hospital of Jilin University

Yunyun Wu

Changchun University of Technology

Jiao Yan

Laboratory of Chemical Biology, Changchun Institute of Applied Chemistry, Chinese Academy of Sciences

Xiaqing Wu

Laboratory of Chemical Biology, Changchun Institute of Applied Chemistry, Chinese Academy of Sciences

Runxiao Zheng

Laboratory of Chemical Biology, Changchun Institute of Applied Chemistry, Chinese Academy of Sciences

yingying Sun

Yanbo Wang

Department of Urology, First Hospital of Jilin University

Haiyuan Zhang (✉ zhangh@ciac.ac.cn)

Laboratory of Chemical Biology, Changchun Institute of Applied Chemistry, Chinese Academy of Sciences <https://orcid.org/0000-0003-4076-1771>

Article

Keywords: Premetastatic niche, Exosome, Pulmonary delivery, Anti-metastasis, IPI549

Posted Date: December 15th, 2021

DOI: <https://doi.org/10.21203/rs.3.rs-1133189/v1>

License: © ⓘ This work is licensed under a Creative Commons Attribution 4.0 International License.

[Read Full License](#)

1 **Pulmonary Delivery of Engineered Exosomes to Suppress Postoperative**
2 **Melanoma Lung Metastasis through Preventing Premetastatic Niche Formation**

3 Xiaoqing Han¹, Luopeng Bi², Yunyun Wu¹, Jiao Yan¹, Xiaoqing Wu¹, Runxiao Zheng¹, Yingying Sun³,
4 Yanbo Wang², Haiyuan Zhang^{1,4*}

5 ¹ Laboratory of Chemical Biology, Changchun Institute of Applied Chemistry, Chinese Academy of
6 Sciences, Changchun 130022 (China)

7 ² Department of Urology, First Hospital of Jilin University, Changchun, 130021 (China)

8 ³ The Key Laboratory of Molecular Epigenetics of Ministry of Education, Institute of Genetics and
9 Cytology, School of Life Sciences, Northeast Normal University, Changchun 130024 (China)

10 ⁴ University of Science and Technology of China, Hefei, Anhui 230026 (China).

11 *Corresponding author:

12 Haiyuan Zhang, Laboratory of Chemical Biology, Changchun Institute of Applied Chemistry, Chinese
13 Academy of Sciences, Changchun 130022 (China); University of Science and Technology of China,
14 Hefei, Anhui 230026 (China); E-mail: zhangh@ciac.ac.cn;

15
16 **Abstract**

17 Premetastatic niche (PMN) is a prerequisite for initiation of tumor metastasis. Targeting prevention
18 of PMN formation in distant organs is becoming a promising strategy to suppress metastasis of primary
19 tumor. Based on “organotropic metastasis”, melanoma tends to metastasize to lungs, where
20 granulocytic myeloid-derived suppressor cells (G-MDSCs) recruitment in lungs significantly
21 contributes to the PMN formation. Herein, functional exosomes (${}^G\text{Exo}^I$) were designed to present
22 pulmonary targeting peptide GFE1 on the membrane and load PI3K γ inhibitor (IPI549) inside, aiming
23 at suppressing postoperative lung metastasis of melanoma. In postoperative mice model, intravenously
24 injected ${}^G\text{Exo}^I$ could significantly accumulate in lungs and release IPI549 to block G-MDSCs
25 recruitment through interfering with CXCLs/CXCR2/PI3K γ signaling. The increased percentages of
26 CD4⁺ T cells and CD8⁺ T cells in lungs could transform microenvironment from immunosuppression to
27 immunostimulation, leading to metastasis inhibition. This study suggests an effective anti-metastasis
28 strategy of targeting prevention of PMN formation through specifically blocking G-MDSCs
29 recruitment.

31 **Key words:** Premetastatic niche, Exosome, Pulmonary delivery, Anti-metastasis, IPI549

32

33 Introduction

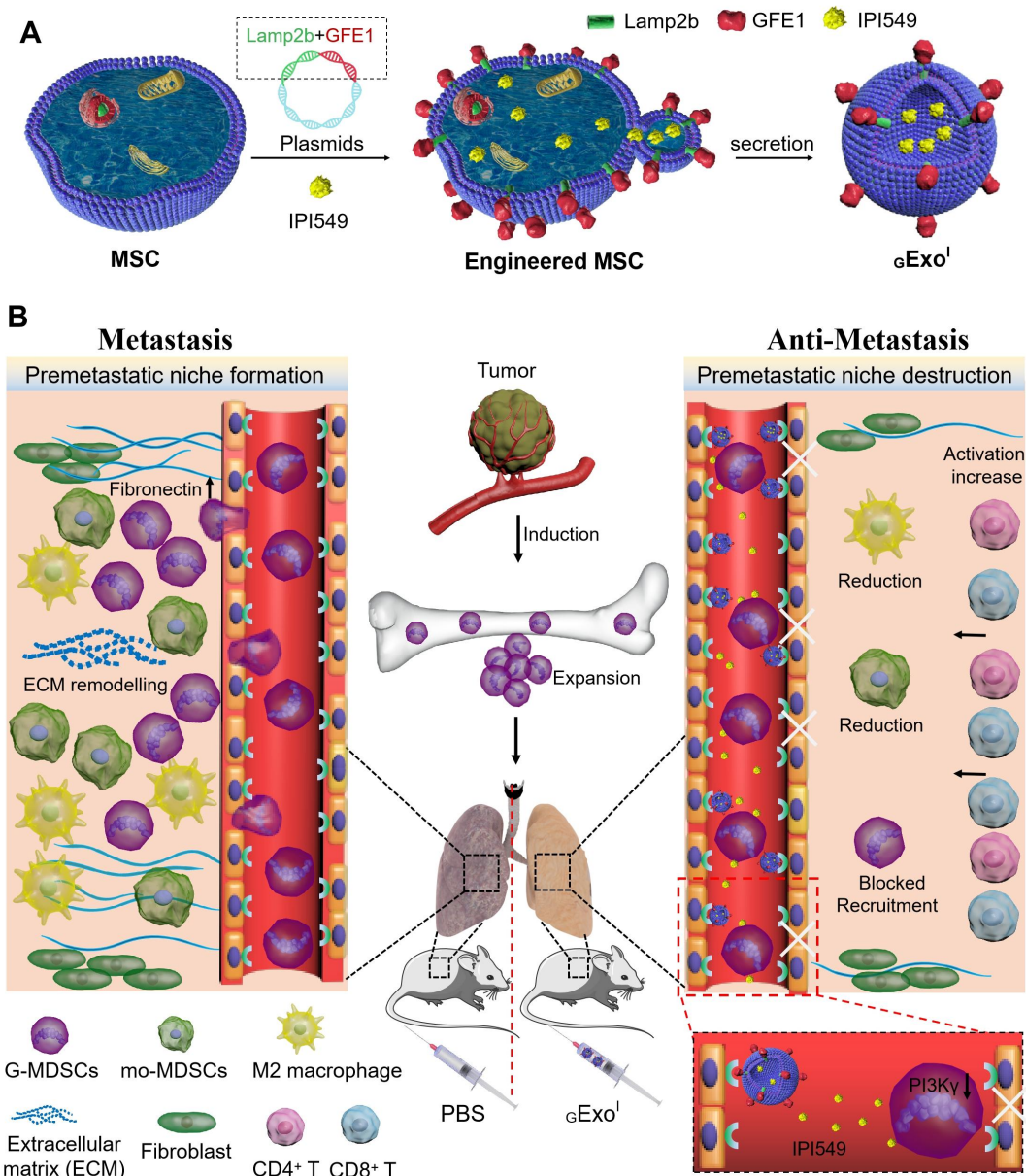
34 Cancer has become the leading cause of threatening human's health, and various traditional
35 treatments including surgery, radiotherapy and chemotherapy have been applied to treat cancer [1].
36 However, due to metastasis, the treatment failure and mortality occurs in more than 90% of individuals
37 with malignant tumors [2-4]. Various anti-metastasis strategies have been developed to improve the
38 treatment of cancer, which mainly focus on the dynamic plasticity of tumor cells, such as the inhibition
39 of migration, adhesion and angiogenesis of tumor cells by drugs[5]. However, as the significant
40 resistance of metastatic tumors to chemotherapy and the limited delivery efficiency of drugs to the
41 tumor metastasis microenvironment, the current treatment of metastasis lacks effectiveness [6].
42 Moreover, surgery as a necessary step in the treatment of solid cancers, may also facilitate the
43 metastatic process by dissemination of tumor cells during the surgical procedure, local and systemic
44 release of growth factors, and cellular immune suppression[7]. It has been well established that organs
45 of future metastasis are not passive receivers of circulating tumor cells, and before metastasis, the
46 microenvironment of the target organs has been altered, such as marrow derived cell aggregation,
47 continuous inflammation and oxygen free radical increase, which is beneficial for creating a suitable
48 niche for metastatic tumor cells colonization [8, 9]. This metastasis-favorable microenvironment
49 created in the distant organs by the primary tumor is defined as the premetastatic niche (PMN) [10-12],
50 which is modified by primary tumor-derived factors and extracellular vesicles, bone marrow-derived
51 cells, stromal cells and the cytokines they produce [13]. Therefore, preventing the PMN formation
52 probably is an effective strategy to inhibit the occurrence of metastasis. However, it is challenging to
53 specifically destroy the PMN formation in organs of future metastasis, and only limited approaches
54 have been exploited [14, 15].

55 Granulocytic myeloid-derived suppressor cells (G-MDSCs) are a major population of immature
56 myeloid cells that accumulate in patients with cancer and appear in the early PMN [16-19]. These
57 G-MDSCs are able to induce immunosuppression, increase vascular permeability and promote the
58 colonization and metastatic growth of disseminated tumor cells in PMN [20-22]. The CXCLs/CXCR2
59 signaling axis plays a vital role in prompting G-MDSCs to enter tissues from bone marrow [23-25]. It
60 has been reported that the primary tumor can recruit CXCR2-positive G-MDSCs by elevating CXCL1

61 in premetastatic liver tissue to form a PMN [26], which suggests that the destruction of
62 CXCLs/CXCR2 signaling axis in G-MDSCs is a potential approach to prevent PMN formation and
63 inhibit the metastasis. Phosphoinositide 3-kinase gamma (PI3K γ) pertains to a signal transducing
64 enzyme that plays an important role in CXCLs/CXCR2 signaling axis. Thus, PI3K- γ inhibition in
65 G-MDSCs may be effective on blocking G-MDSCs recruitment for PMN elimination. However, since
66 PI3K- γ is also a critical determinant of the proportion of neutrophil chemotaxis [27], non-specific
67 PI3K γ inhibition would cause the obstacle of the recruitment of neutrophils to non-tumor metastasis
68 organs, resulting in severe immune system defects in the body. Therefore, realization of specific PI3K- γ
69 inhibition in G-MDSCs will become a safe and feasible approach for inhibiting PMN formation and
70 further preventing the metastasis.

71 Clinical observations suggest that most cancers usually can metastasize to specific organs, so called
72 “organotropic metastasis”. For examples, melanoma tends to metastasize to lungs; colorectal cancer
73 tends to metastasize to livers; prostate cancers selectively metastasize to bone [28-30]. Such
74 phenotypes offer opportunities to prevent tumor metastasis by specific blocking PMN formation in the
75 organs of future metastasis. Despite the promising anti-metastasis potential of blocking PMN formation,
76 its clinical application is restricted by the lack of organ specificity after systemic administration.
77 Development of biocompatible and organ-targeting drug delivery system will be required. Exosomes
78 naturally secreted by various cell types is membrane-enclosed vesicles with sizes of 30–200 nm [31].
79 Those exosomes obtained from the patient's own cells have desirable biocompatibility, low
80 immunogenicity and prolonged systemic circulating ability [32-34]. While various exosomes have been
81 used as carriers for anti-tumor metastasis therapy, the affinity of exosomes to mother cells is not
82 sufficient for exosomes to specifically aggregate in one organ of the body [35-37]. Current methods
83 which endow exosomes with the specific targeting ability involve genetic manipulation of the producer
84 cells or chemical conjugation of peptides to the surface of exosomes [32, 38-41]. Therefore, based on
85 above methods, organ-specific targeting exosomes can be obtained with organ-targeting peptides.
86 Furthermore, the engineering organ-targeted exosomes can site-specifically deliver drugs to specific
87 metastasis site, potentially directionally inhibiting the PMN formation in organs of premetastasis.

88



89

90 Figure 1 Schematic illustration for anti-tumor metastatic effects of gExo^I. **a** Preparation of gExo^I from
 91 MSCs that were transfected with the recombinant plasmid encoding Lamp2b-GFE1 fusion protein and
 92 incubated with the PI3K γ inhibitor, IPI549. **b** Process of pulmonary delivery of gExo^I through GFE1
 93 binding to the surface of pulmonary vascular endothelial cells and prevention of PMN formation
 94 through IPI549-mediated blockage of G-MDSCs recruitment. The decreased percentages of monocytic
 95 myeloid-derived suppressor cells (mo-MDSCs) and M2 phenotype macrophage and the increased
 96 percentages of CD4⁺ T cells and CD8⁺ T cells in lungs could transform microenvironment from
 97 immunosuppression to immunostimulation, blocking the lung metastasis of melanoma.

98

99 In the present study, functional exosomes were engineered for targeted delivery of the PI3K γ

100 inhibitor (IPI549) to lung of a melanoma mouse model, aiming at preventing the PMN formation and
101 suppressing postoperative lung metastasis of melanoma. Mesenchymal stem cells (MSCs) from the
102 bone marrow of mice were used to produce exosomes with low immunogenicity [42]. The plasmid
103 which expressed lysosome-associated membrane glycoprotein 2b (Lamp2b), an exosomal membrane
104 protein [32], fused with GFE1 (CGFECVRQCPERC) targeting peptide for pulmonary vascular
105 endothelial cells [43] on the extra-exosomal N terminus of Lamp2b was constructed. Then, the
106 corresponding expression vectors were transfected into MSCs to produce Lamp2b-GFE1 fusion protein,
107 which was exposed on the surface of exosomes. The transfected MSCs were purified and incubated
108 with IPI549 (a PI3K γ inhibitor). The GFE-1-positive and IPI549-loaded exosomes (${}^{\text{G}}\text{Exo}^{\text{I}}$) were
109 purified from cell culture supernatants (**Fig.1a**). After intravenously injected into a mouse model of
110 melanoma, ${}^{\text{G}}\text{Exo}^{\text{I}}$ could accumulate at the lung through GFE1 binding to the surface of pulmonary
111 vascular endothelial cells, and gradually release IPI549 to block the G-MDSCs recruitment and
112 preventing the PMN formation, leading to suppression of the lung metastasis of melanoma (**Fig. 1b**).
113 Collectively, this is the first proof-of-concept attempt to block tumor metastasis based on the tumor
114 metastasis organotropism and the local PMN inhibition, which will serve as a powerful strategy for
115 postoperative metastasis of tumor.

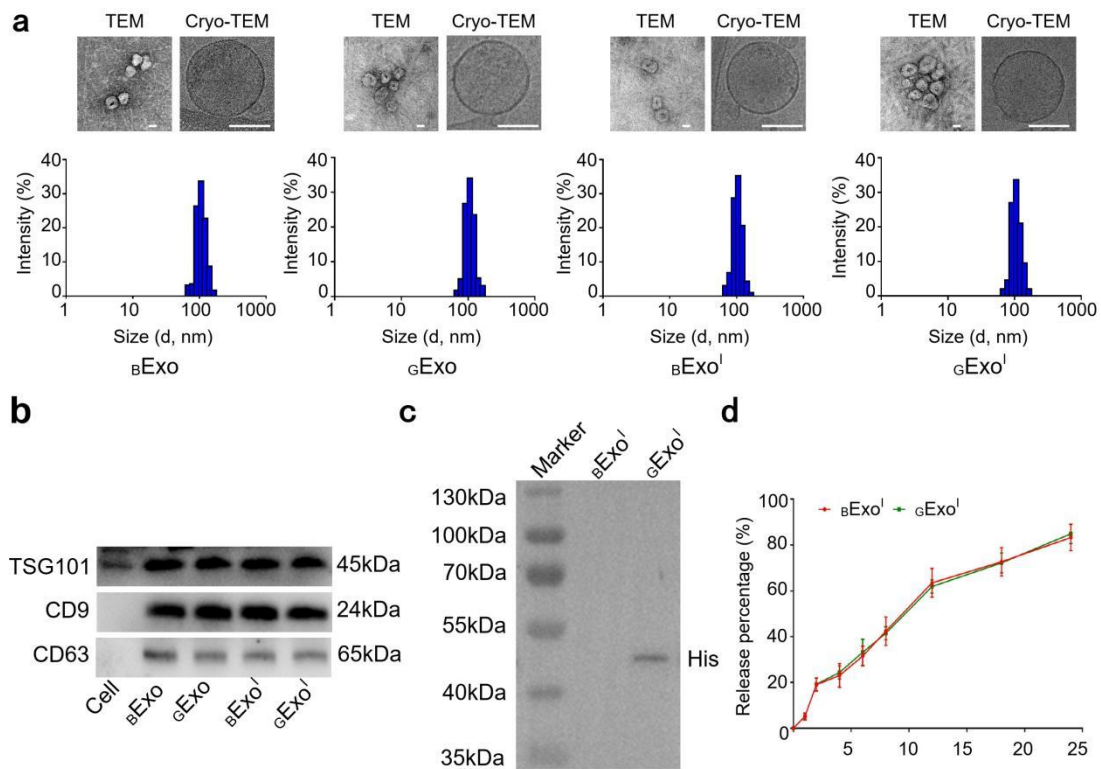
116

117 **Results and discussion**

118 **1. Characterization of ${}^{\text{G}}\text{Exo}^{\text{I}}$**

119 MSCs were isolated from the bone marrow of mice, which were positive for CD29, CD44, and
120 CD105, but negative for CD34 and CD45 (**Supplementary Fig. 1**). The purity of MSCs in culture was
121 up to 93%. To generate GFE1-positive exosomes, we fused the GFE1 peptide to the extra-exosomal N
122 terminus of murine Lamp2b protein by introducing the pEGFP-C1-GFE1-Lamp2b plasmid into MSCs.
123 The level of GFE1-Lamp2b mRNA was assessed at 24 h after transfection using reverse transcription
124 polymerase chain reaction (PCR). Relative to untransfected MSCs, the transfected MSCs expressed a
125 high level of GFE1-Lamp2b message RNA (**Supplementary Fig. 2**). Meanwhile, the transfected MSCs
126 were further incubated with IPI549 for another 24 h. Then, GFE-1 positive and IPI549-loaded
127 exosomes (${}^{\text{G}}\text{Exo}^{\text{I}}$) were achieved from the culture supernatants through ultracentrifugation. The GFE-1
128 negative exosomes (${}^{\text{B}}\text{Exo}$), GFE-1 positive exosomes (${}^{\text{G}}\text{Exo}$) and GFE-1 negative but IPI549-loaded
129 exosomes (${}^{\text{B}}\text{Exo}^{\text{I}}$) were similarly prepared as controls. Transmission electron microscopy (TEM) and

130 cryo-TEM (**Fig. 2a**) images clearly revealed typical exosome structures of ${}_{\text{B}}\text{Exo}$, ${}_{\text{G}}\text{Exo}$, ${}_{\text{B}}\text{Exo}^{\text{I}}$ and ${}_{\text{G}}\text{Exo}^{\text{I}}$.
 131 Dynamic light scattering (DLS) analysis showed that ${}_{\text{B}}\text{Exo}$, ${}_{\text{G}}\text{Exo}$, ${}_{\text{B}}\text{Exo}^{\text{I}}$ and ${}_{\text{G}}\text{Exo}^{\text{I}}$ had similar
 132 hydrodynamic sizes of 116 ± 3.3 , 109 ± 4.9 , 110.4 ± 5.6 and 114.3 ± 4.1 nm respectively (**Fig. 2a**). Western
 133 blot analysis revealed that ${}_{\text{B}}\text{Exo}$, ${}_{\text{G}}\text{Exo}$, ${}_{\text{B}}\text{Exo}^{\text{I}}$ and ${}_{\text{G}}\text{Exo}^{\text{I}}$ contained the abundant exosome marker
 134 proteins, such as TSG101, CD9 and CD63 (**Fig. 2b**), suggesting that the successful isolation of
 135 exosomes from MSCs. To confirm GFE-1 was located on the surface of exosomes, the binding ability
 136 of ${}_{\text{B}}\text{Exo}^{\text{I}}$ and ${}_{\text{G}}\text{Exo}^{\text{I}}$ to His-tagged recombinant DPEP1 that is the receptor for the lung-targeting peptide
 137 GFE1 was detected by assessing the levels of His-tag in ${}_{\text{B}}\text{Exo}^{\text{I}}$ and ${}_{\text{G}}\text{Exo}^{\text{I}}$. Western blot analysis showed
 138 that ${}_{\text{G}}\text{Exo}^{\text{I}}$ could strongly bind to DPEP1, but no detectable binding was observed in ${}_{\text{B}}\text{Exo}^{\text{I}}$ group (**Fig.**
 139 **2c**), supporting the existence of GFE1 on the surface of ${}_{\text{G}}\text{Exo}^{\text{I}}$. The loading capacities of IPI549 in the
 140 ${}_{\text{G}}\text{Exo}^{\text{I}}$ and ${}_{\text{B}}\text{Exo}^{\text{I}}$ were determined as 17.79 and 15.59%, respectively, and the IPI549 release profile was
 141 investigated by high performance liquid chromatography (HPLC). The results implied that both ${}_{\text{B}}\text{Exo}^{\text{I}}$
 142 and ${}_{\text{G}}\text{Exo}^{\text{I}}$ showed similar sustained release profiles, and approximately 83.26 ± 1.89 % of total IPI549
 143 were slowly released from both exosomes within 24 h. It seems the introduction of GFE1 did not affect
 144 the drug release capability of exosomes (**Fig. 2d**).



145
 146 **Figure 2. Characterization of exosomes.** **a** TEM and Cryo-TEM images as well as hydrodynamic
 147 sizes of ${}_{\text{B}}\text{Exo}$, ${}_{\text{G}}\text{Exo}$, ${}_{\text{B}}\text{Exo}^{\text{I}}$ and ${}_{\text{G}}\text{Exo}^{\text{I}}$. Scale bar, 50 nm. **b** Western blot analysis of TSG101, CD9 and

148 CD63 from IPI549-primed MSCs, ${}_{\text{B}}\text{Exo}$, ${}_{\text{G}}\text{Exo}$, ${}_{\text{B}}\text{Exo}^{\text{I}}$ and ${}_{\text{G}}\text{Exo}^{\text{I}}$. **c** Western blot analysis of ${}_{\text{B}}\text{Exo}^{\text{I}}$ and
149 ${}_{\text{G}}\text{Exo}^{\text{I}}$ binding with DPEP1 using an anti-6x His-tag. **d** IPI549 release profiles of ${}_{\text{B}}\text{Exo}^{\text{I}}$ and ${}_{\text{G}}\text{Exo}^{\text{I}}$ in the
150 phosphate-buffered saline (PBS) over 24 hours. Data are expressed as means \pm SD.

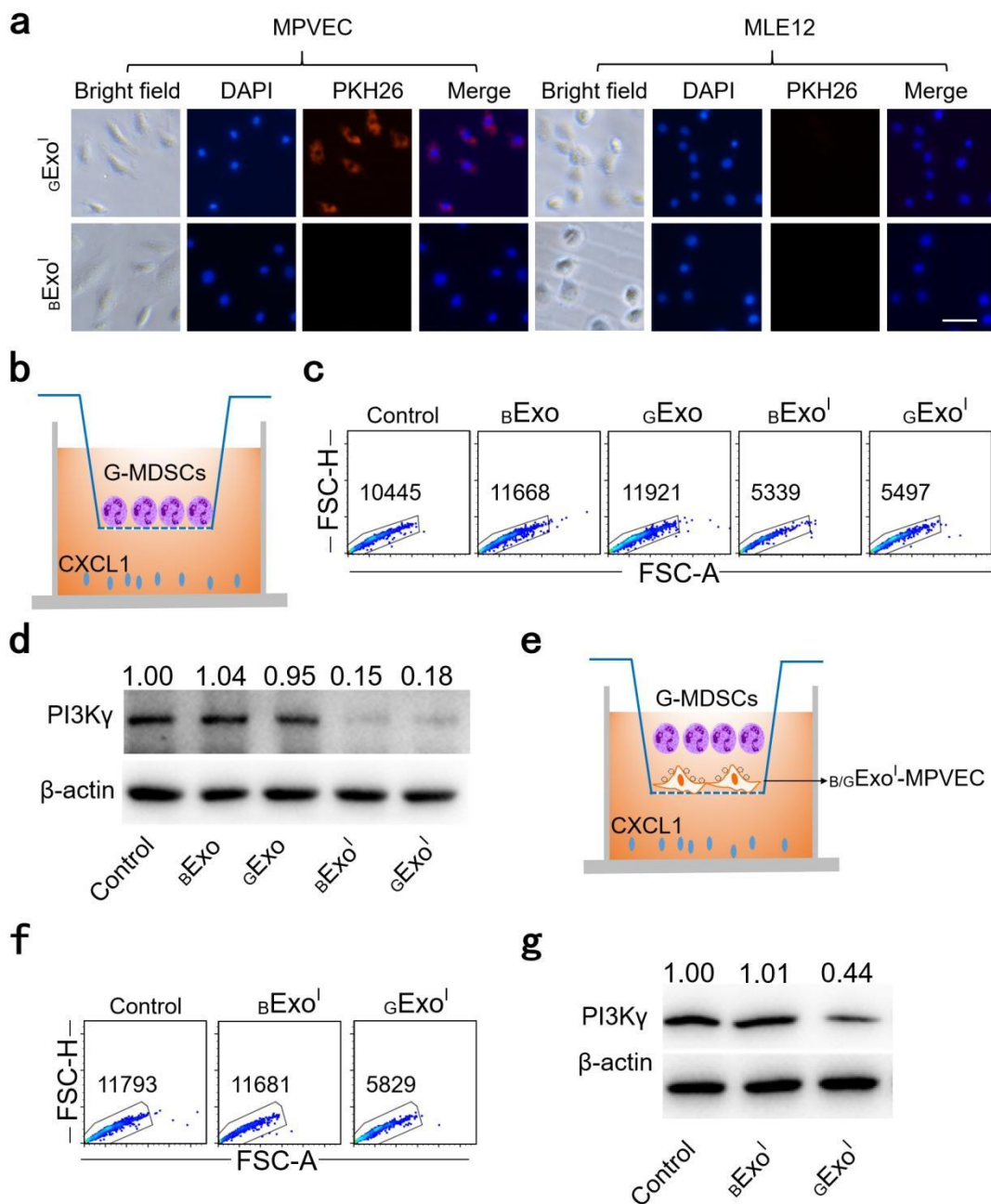
151

152 **2. Cellular tropism of ${}_{\text{G}}\text{Exo}^{\text{I}}$**

153 The *in vitro* biocompatibility of ${}_{\text{G}}\text{Exo}^{\text{I}}$ was assessed by CCK8 assay in murine macrophage cells
154 (RAW 264.7) and human umbilical vein endothelial cells (HUVEC). After 24 h exposure to different
155 concentrations of ${}_{\text{B}}\text{Exo}^{\text{I}}$ and ${}_{\text{G}}\text{Exo}^{\text{I}}$, the viability of cells was found to be weakly affected
156 (**Supplementary Fig. 3 and 4**). GFE1 peptide has been reported to efficiently target pulmonary
157 vascular [44]. In order to explore the ability of ${}_{\text{G}}\text{Exo}^{\text{I}}$ targeting to pulmonary vascular, pulmonary
158 vascular endothelial cells (MPVEC) and lung epithelial cells (MLE12) were chosen to be treated with
159 PKH26 (a red fluorescent dye)-labeled ${}_{\text{B}}\text{Exo}^{\text{I}}$ and ${}_{\text{G}}\text{Exo}^{\text{I}}$. Cellular fluorescence images showed that
160 ${}_{\text{G}}\text{Exo}^{\text{I}}$ could be efficiently taken into MPVEC rather than MLE12, presenting potent red fluorescence,
161 while ${}_{\text{B}}\text{Exo}^{\text{I}}$ had low uptake in both MPVEC and MLE12 (**Fig. 3a**), which reveals the higher affinity of
162 ${}_{\text{G}}\text{Exo}^{\text{I}}$ compared with ${}_{\text{B}}\text{Exo}^{\text{I}}$ toward the pulmonary blood vessels.

163 The inhibition effect of ${}_{\text{G}}\text{Exo}^{\text{I}}$ on G-MDSCs migration was investigated in a G-MDSCs/CXCL1
164 transwell system, where G-MDSCs were cultured in the upper chamber and CXCL1 as chemokine to
165 recruit G-MDSCs was loaded in the lower chamber (**Fig. 3b**). Various exosomes (${}_{\text{G}}\text{Exo}$, ${}_{\text{B}}\text{Exo}$, ${}_{\text{B}}\text{Exo}^{\text{I}}$
166 and ${}_{\text{G}}\text{Exo}^{\text{I}}$) were incubated with G-MDSCs for 4 h in the upper chamber. G-MDSCs recruited into the
167 lower chamber were counted by flow cytometry. The results revealed that the numbers of G-MDSCs
168 migration in ${}_{\text{B}}\text{Exo}^{\text{I}}$ and ${}_{\text{G}}\text{Exo}^{\text{I}}$ group were less than those in ${}_{\text{B}}\text{Exo}$ and ${}_{\text{G}}\text{Exo}$ group (**Fig. 3c**), and the
169 percentages of migrated G-MDSCs in ${}_{\text{B}}\text{Exo}^{\text{I}}$ and ${}_{\text{G}}\text{Exo}^{\text{I}}$ groups were only 8.50 ± 2.04 and 7.77 ± 1.76 %
170 (**Supplementary Fig. 5**), and the PI3K γ expression of G-MDSCs in the upper chamber was
171 down-regulated after both ${}_{\text{B}}\text{Exo}^{\text{I}}$ and ${}_{\text{G}}\text{Exo}^{\text{I}}$ treatments (**Fig. 3d**). All these results suggest IPI549-loaded
172 exosomes can significantly inhibit the migration of G-MDSCs. Furthermore, to investigate the targeted
173 transporting ability of ${}_{\text{G}}\text{Exo}^{\text{I}}$ to pulmonary vascular endothelial cells, a G-MDSCs/MPVEC/CXCL1
174 transwell system was established, while G-MDSCs and ${}_{\text{B}}\text{Exo}^{\text{I}}$ - or ${}_{\text{G}}\text{Exo}^{\text{I}}$ -treated MPVEC were cultured
175 in the upper chamber while CXCL1 was in the lower chamber (**Fig. 3e**). Because ${}_{\text{G}}\text{Exo}^{\text{I}}$ could target to
176 MPVEC but ${}_{\text{B}}\text{Exo}^{\text{I}}$ could not, we hypothesized only ${}_{\text{G}}\text{Exo}^{\text{I}}$ -treated MPVEC carried IPI549 but
177 ${}_{\text{B}}\text{Exo}^{\text{I}}$ -treated MPVEC did not. Encouragingly, the number of G-MDSCs migration in ${}_{\text{G}}\text{Exo}^{\text{I}}$ -treated

178 MPVEC group was decreased but the number of β Exo^l-treated MPVEC group was not (**Fig. 3f**), and
 179 the percentage of migrated G-MDSCs in α Exo^l-treated MPVEC group decreased to $11.67 \pm 1.25\%$
 180 (**Supplementary Fig. 6**), which is ascribed to the targeted release of IPI549 of α Exo^l in MPVEC.
 181 Moreover, the PI3K γ expression in G-MDSCs in the upper chamber also was down-regulated in
 182 α Exo^l-treated MPVEC group (**Fig. 3g**). All above results suggest that α Exo^l can mediate the targeted
 183 delivery of IPI549 to pulmonary vascular endothelial cells and durably inhibit the migration of
 184 G-MDSCs by downregulating PI3K γ .



185

186 **Figure 3. Cellular tropism of α Exo^l.** **a** Cellular uptake of α Exo^l and β Exo^l as assessed by fluorescence

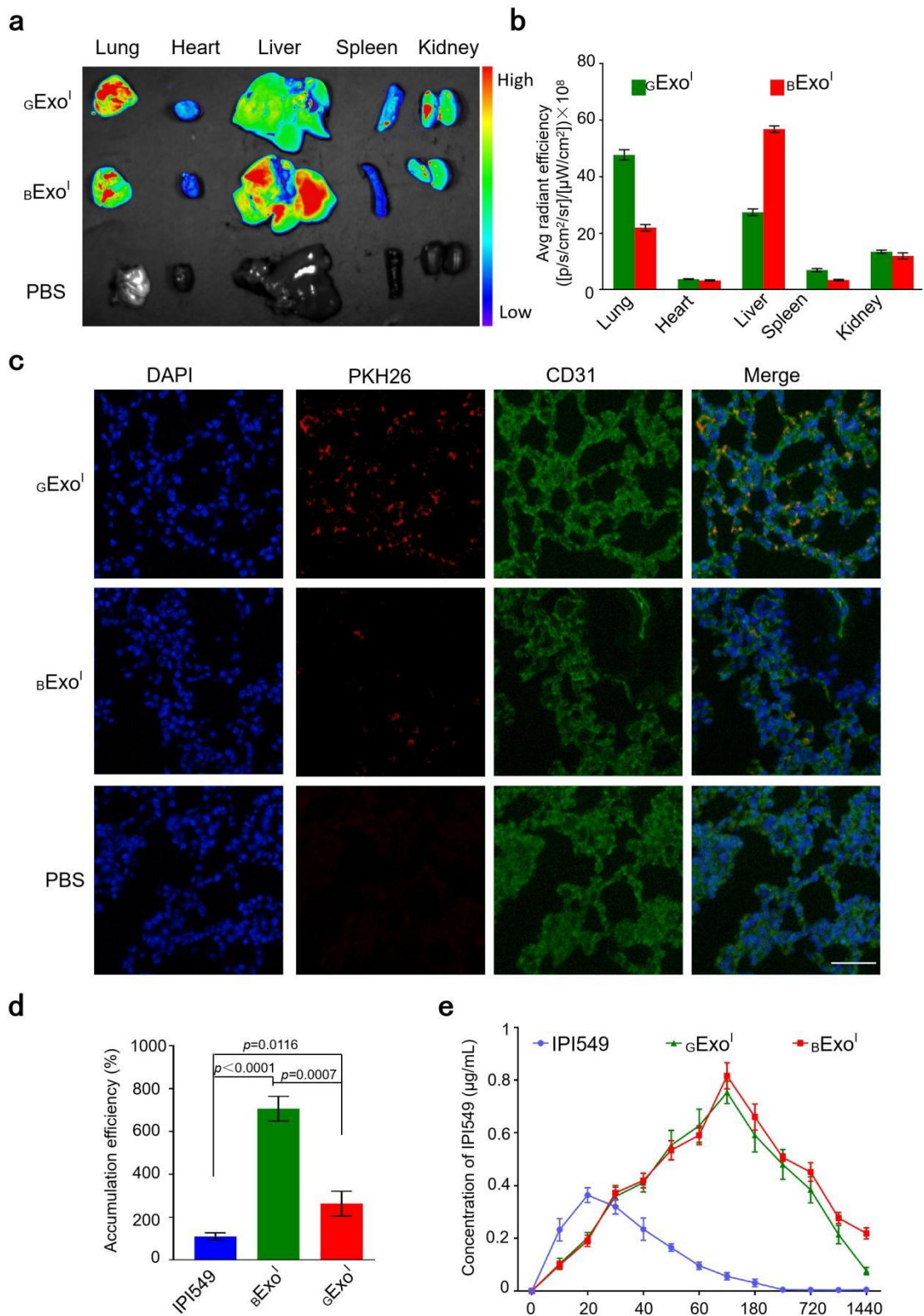
187 microscopy. DAPI was used to stain the nuclei (blue). $_{B}Exo$ and $_{G}Exo$ were stained with PKH26 (red).
188 Scale bar, 50 μ m. **b** Establishment of G-MDSCs/CXCL1 transwell system. **c** Migration number of
189 G-MDSCs in G-MDSCs/CXCL1 transwell system as assessed by flow cytometry. **d** Western blot
190 analysis of PI3K γ expression in G-MDSCs of G-MDSCs/CXCL1 transwell system. **e** Establishment of
191 G-MDSCs/MPVEC/CXCL1 transwell system. **f** Migration number of G-MDSCs in G-MDSCs/CXCL1
192 transwell system as assessed by flow cytometry. **g** Western blot analysis of PI3K γ expression in
193 G-MDSCs in G-MDSCs/MPVEC/CXCL1 transwell system. Data are expressed as means \pm SD.

194

195 **3. Enhanced pulmonary targeting ability and bioavailability of $_{G}Exo^I$**

196 Encouraged by above *in vitro* results, the *in vivo* biodistribution of $_{G}Exo^I$ was then taken further
197 investigation. The pKH26-labeled $_{B}Exo^I$ or $_{G}Exo^I$ was injected intravenously to healthy C57BL/6 mice,
198 and the fluorescence images of the major organs showed that $_{B}Exo^I$ and $_{G}Exo^I$ mainly distributed in the
199 liver, kidney and lung, among which $_{G}Exo^I$ had the highest accumulation in the lung while $_{B}Exo^I$ had
200 the highest one in the liver (**Fig. 4a and b**). This result reveals the excellent pulmonary targeting ability
201 of $_{G}Exo^I$, which is attributed to GFE1 peptide on the surface of $_{G}Exo^I$. To further determine the detailed
202 distribution of $_{B}Exo^I$ and $_{G}Exo^I$ in the lung tissue, the lung slices were stained with FITC-CD31, a
203 vascular endothelial cell marker. Fluorescence microscopy image showed that the red fluorescence of
204 pKH26-labeled $_{G}Exo^I$ was bound to the pulmonary vasculature, however, only a few of pKH26-labeled
205 $_{B}Exo^I$ distributed irregularly throughout the lung slice (**Fig. 4c**). Next, the biodistributions of IPI549 in
206 different organs of mice was quantitatively analyzed by HPLC. Treatments with $_{B}Exo^I$ or $_{G}Exo^I$ could
207 increase the accumulation of IPI549 in the liver (**Supplementary Fig. 7**), kidney (**Supplementary Fig.**
208 **8**) and lungs (**Fig. 4d**) of mice as compared with treatment with free IPI549, and more importantly,
209 $_{G}Exo^I$ compared with $_{B}Exo^I$ could more significantly increase the accumulation of IPI549 in the lung.
210 This result demonstrates $_{G}Exo^I$ can enhance the accumulation of IPI549 in the pulmonary vasculature
211 by binding to vascular endothelial cells in the lung. To evaluate the pharmacokinetic profile of IPI549,
212 the time-dependent IPI549 plasma concentration of mice injected with free IPI549 or exosomes ($_{B}Exo^I$
213 and $_{G}Exo^I$) was investigated by HPLC. **Fig. 4e** showed that the maximum IPI549 plasma concentration
214 (C_{max}) of mice with free IPI549 treatment peaked at 20 min post-injection, which was 0.38 μ g mL $^{-1}$,
215 and then decreased rapidly. The C_{max} of mice with $_{B}Exo^I$ or $_{G}Exo^I$ treatment peaked at 2 h
216 post-injection and was improved to 0.72 μ g mL $^{-1}$ (for $_{G}Exo^I$) or 0.78 μ g mL $^{-1}$ (for $_{B}Exo^I$). Compared

217 with free IPI549, both $gExo^I$ and $bExo^I$ also contributed to the higher bioavailability and slower
 218 metabolism rate.



219

220 **Figure 4. Pulmonary targeting of $gExo^I$.** a Ex vivo fluorescence images of the major organs (heart,

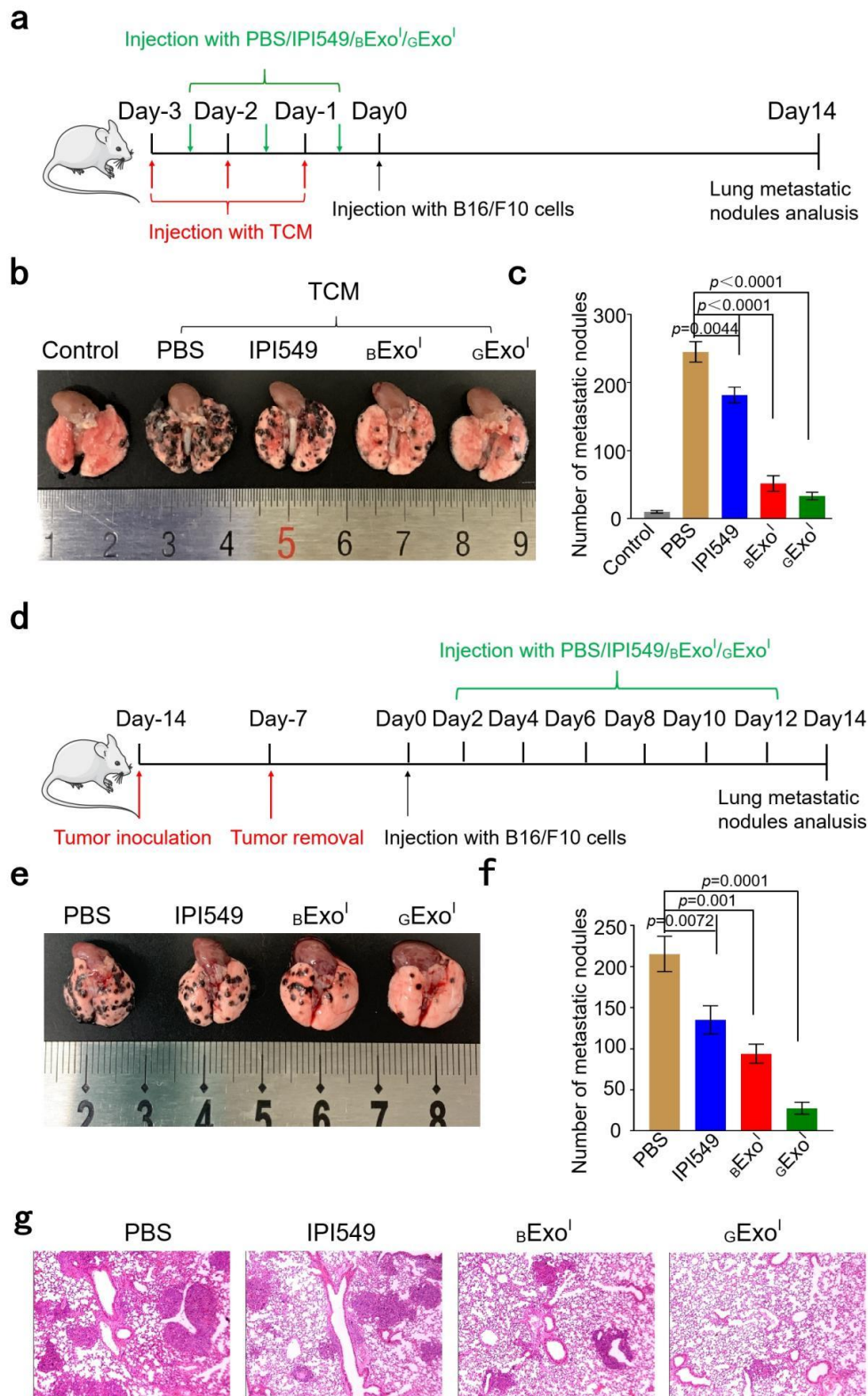
221 liver, spleen, lung, and kidney) from mice at 24 h postinjection with PBS, PKH26-labeled $bExo^I$ or

222 GExo^{I} , respectively. **b** Semi-quantitation of fluorescence intensity of major organs. **c**
223 Immunofluorescent images of lung tissues stained by the vascular endothelial cells marker CD31
224 (green). Scale bar, 100 μm . **d** Tissue distribution of IPI549 in the lung of mice treated as described in
225 Figure 4a. **e** Plasma concentration-time curve of IPI549 in mice plasma after single intravenous
226 injection of free IPI549, BExo^{I} or GExo^{I} (equivalent to the concentration of 0.2 mg IPI549/kg mouse).
227 Data are expressed as means \pm SD. n = 5 biologically independent animals per group.

228

229 **4. Therapeutic efficacy of GExo^{I} to suppress postoperative metastasis of melanoma**

230 The primary tumor tissue can induce the spontaneous development of PMN, and tumor metastasis
231 will occur once the PMN is formed, even if the tumor in situ is surgically removed [10]. To evaluate the
232 inhibitory efficacy of GExo^{I} against PMN formation in the lung, B16/F10 cells-derived tumor
233 conditioned medium (TCM) stimulating mice model was established. The TCM using as tumor
234 secretions was intravenously injected into normal C57BL/6 mice, and free IPI549, BExo^{I} or GExo^{I} was
235 injected intravenously at the same time, followed by intravenous injection of B16/F10 cells (**Fig. 5a**).
236 The PMN characteristic gene expression in lungs, including Bv8, S100a8, S100a9, and MMP9, which
237 are reported to promote tumor cell invasion, migration, and colonization in the metastatic site [45],
238 were assessed by real-time PCR. The result showed the treatment with TCM alone significantly
239 increased the expression of Bv8, S100a8, S100a9, and MMP9 in the lung than that of normal mice
240 (**Supplementary Fig. 9**). However, additional treatment with free IPI549, BExo^{I} or GExo^{I} decreased
241 their expression, where GExo^{I} exhibited the most potent performance, suggesting GExo^{I} can effectively
242 inhibit lung PMN establishment. Furthermore, the metastatic nodules in the lung of mice were counted.
243 Only TCM-treated mice showed the most metastatic nodules, accelerating the metastasis, but the
244 further treatment with IPI549, BExo^{I} or GExo^{I} induced the reduced metastatic nodules, showing
245 inhibited metastasis (**Fig. 5b and 5c**). Importantly, GExo^{I} triggered the least metastatic nodules,
246 exhibiting the best inhibitory activity against metastasis. All above results indicate that GExo^{I} can
247 significantly inhibit tumor metastasis by blocking PMN formation in the lung.



248

249 **Figure 5. Suppressed metastasis by g Exo¹.** **a** Treatment schedule and timeline for TCM stimulation,
 250 treatments with various drug formulations, and lung metastasis evaluation. Days were recounted from
 251 day 0 after all TCM stimulations and treatments. **b** The metastatic nodules in the lungs of control mice
 252 without injection with TCM and mice injected with TCM + PBS, TCM + IPI549, TCM + β Exo¹, or

253 TCM + gExo^{I} . All mice were sacrificed at 2 weeks after a tail vein injection with B16F10 cells. The
254 black point represented visible metastatic nodules in the lung. **c** Average number of macroscopic lung
255 metastatic nodules in mice treated as in Figure 5B. **d** Schematic illustration of postoperative lung
256 metastasis models and therapies. **e** Images of the lung tissue from postoperative lung metastasis mice
257 treated with PBS, IPI549, BExo^{I} or gExo^{I} . **f** Average number of macroscopic lung metastatic nodules in
258 mice treated as described in Figure 5E. **g** H&E-stained tissue sections of lung excised at the end of
259 treatments. Scale bar, 100 μm . For **e-g**, mice whose subcutaneous tumors (100 mm^3) were completely
260 excised were intravenously injected with B16/F10 cells at 7 days post-surgery. PBS, free IPI549, BExo^{I}
261 or gExo^{I} was injected intravenously to the mice every two days after injection with B16/F10 cells. All
262 mice were sacrificed at 2 weeks after intravenous injection with B16F10 cells. Data are expressed as
263 means \pm SD. $n = 5$ biologically independent animals per group.

264

265 To finally determine whether gExo^{I} can prevent the postoperative tumor metastasis, the postoperative
266 lung metastasis model was generated in C57BL/6 mice. B16/F10 cells were first subcutaneously
267 injected in C57BL/6 mice. When the tumor volume reached about 100 mm^3 , the tumor was completely
268 excised, followed by intravenous injection of B16/F10 cells at 7 days post-surgery. PBS, free IPI549 or
269 the exosomes (BExo^{I} and gExo^{I}) were injected intravenously to the mice every two days after injection
270 of B16/F10 cells (**Fig. 5d**). Compared to the mice treated with free IPI549, the number of macroscopic
271 metastatic nodules of both exosomes-treated mice was dramatically decreased, where gExo^{I} still
272 showed more significant metastases inhibition than BExo^{I} (**Fig. 5e and 5f**). From the hematoxylin-eosin
273 (H&E) staining of the lung metastatic lesions (**Fig. 5g**), metastatic nodules and inflammation could be
274 distinctly detected in PBS-treated mice. While treatments with free IPI549 or BExo^{I} could decrease the
275 nodules and inflammation in the lung, there was barely the nodules and inflammation in the lung of
276 gExo^{I} -treated mice, indicating the remarkable anti-metastatic efficacy of gExo^{I} .

277

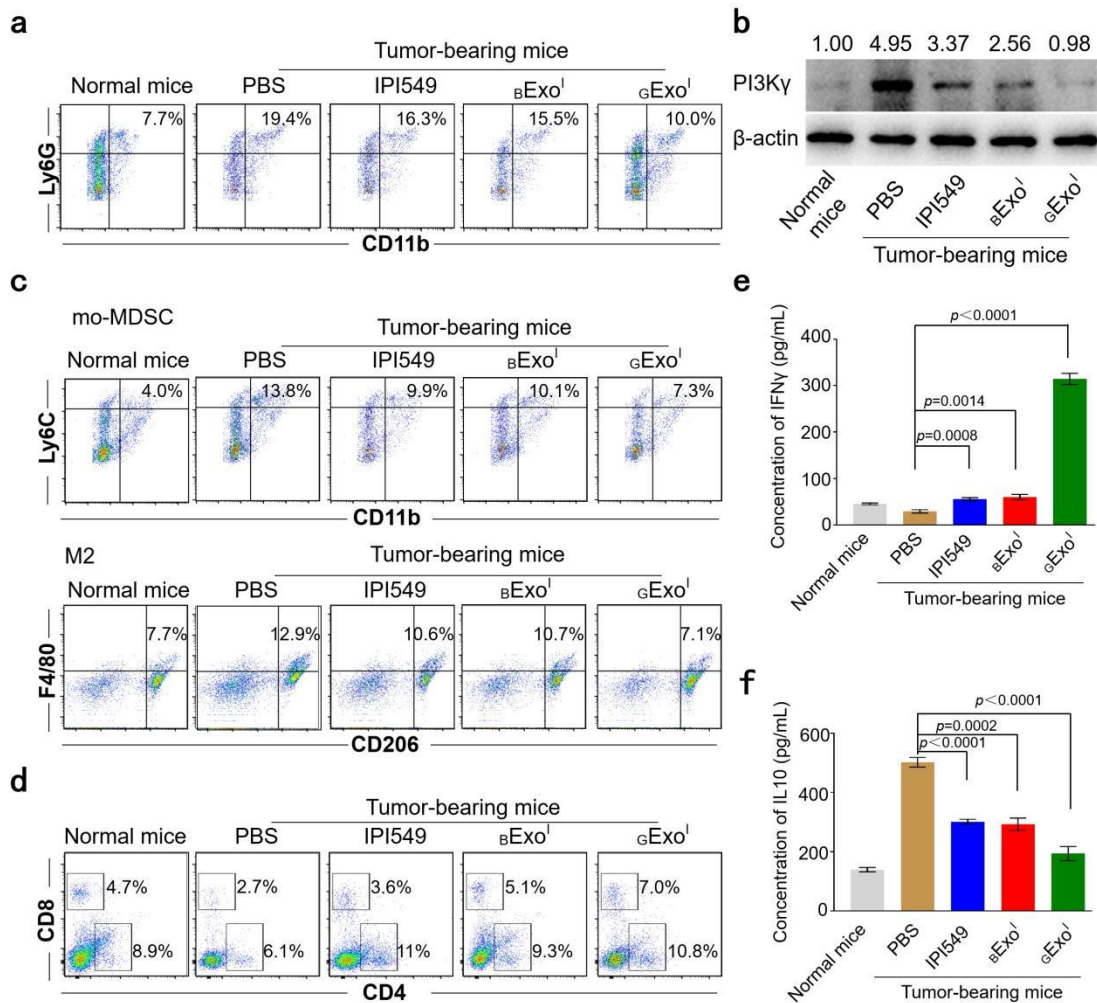
278 **5. Inhibited G-MDSCs accumulation in the lung by gExo^{I} to prevent PMN formation**

279 It has been demonstrated that G-MDSCs play a vital role in promoting metastases in tumor-bearing
280 mice, and their accumulation in premetastatic organs is a complex process that is regulated mainly by
281 CXCLs factors (CXCL1, CXCL2, CXCL5, and CXCL8)[23]. Because of the wide range of factors, it
282 is difficult to achieve anti-tumor metastasis by simply inhibiting the expression of a certain factor [46].

283 Here, we first design an anti-accumulation strategy to inhibit the chemotactic migration of G-MDSCs
284 into the lung by blocking the CXCLs/CXCR2/PI3K γ signaling of G-MDSCs. To investigate the
285 influence of GExo^{I} on G-MDSCs recruitment before PMN formation, the percentage of G-MDSCs
286 (CD11b $^+$ Ly6G $^+$) in the lung of the postoperative lung metastasis mice model was analyzed by flow
287 cytometry. **Fig. 6a and Supplementary Fig. 10** show that IPI549 and BExo^{I} could reduce the
288 percentage of G-MDSCs in premetastatic lungs, but GExo^{I} even decreased the percentage close to the
289 normal level of healthy mice, which is because on the one hand GExo^{I} has a longer circulation time than
290 IPI549, capable of more effectively blocking the chemotactic migration of G-MDSCs, and on the other
291 hand, GExo^{I} has a higher drug delivery efficiency than BExo^{I} , thus releasing the stronger
292 anti-recruitment ability. Moreover, the expression of PI3K γ in G-MDSCs from premetastatic lungs of
293 mice with different treatments was observed to show the same trend as the percentage of G-MDSCs did
294 (**Fig. 6b**).

295 G-MDSCs can suppress the immunity by perturbing both innate and adaptive immune responses,
296 such as promoting the generation of monocytic myeloid-derived suppressor cells (mo-MDSCs),
297 skewing macrophage towards an M2 phenotype, and blocking the activation and proliferation of CD8 $^+$
298 T cells [47, 48]. Then, the impact of GExo^{I} on the function of G-MDSCs was further assessed. The
299 percentages of the major immune cells in the lung tissues were detected by flow cytometry in the lung
300 of the postoperative lung metastasis mice model. The percentages of mo-MDSCs (CD11b $^+$ Ly6C $^+$) and
301 M2 macrophages (F4/80 $^+$ CD206 $^+$) in the lungs of the GExo^{I} -treated mice decreased most significantly,
302 which probably is because the decreased G-MDSCs could cause the decrease of mo-MDSCs generation
303 and impairment of macrophage polarization towards an M2 phenotype (**Fig. 6c and Supplementary**
304 **Fig. 11**). The percentage of CD4 $^+$ T cells in the lungs of free IPI549-, BExo^{I} - and GExo^{I} -treated mice
305 were increased, compared with that of PBS-treated mice (**Fig. 6d and Supplementary Fig. 12**),
306 indicating that the reduction of G-MDSCs can achieve the remodeling of acquired immunity. Moreover,
307 the percentage of CD8 $^+$ T cells in the lungs of the GExo^{I} -treated mice increased most significantly (**Fig.**
308 **6d and Supplementary Fig. 13**). Based on the above results, the composition ratio of various immune
309 cells in the premetastatic lung was changed by the reduction of G-MDSCs. IFN γ coordinates multiple
310 protective functions to enhance the immune response to infection and cancer [49] and IL-10 is a
311 pleiotropic anti-inflammatory cytokine that induces immunosuppression and assists in escape from
312 tumor immune surveillance [50]. The lung homogenate of postoperative lung metastasis mice model

313 was collected at the end of various treatments for detection of IFN γ and IL10 by enzyme-linked
 314 immunosorbent assay (ELISA). As shown in **Figure 6e and f**, α Exo^l could induce the highest level of
 315 IFN γ among the four treatment groups and the level of IL10 close to that in healthy mice, due to the
 316 targeted IPI549 delivery ability of α Exo^l. Taken all together, the reduction of G-MDSCs by α Exo^l can
 317 create an immune activated microenvironment in the premetastatic lung.



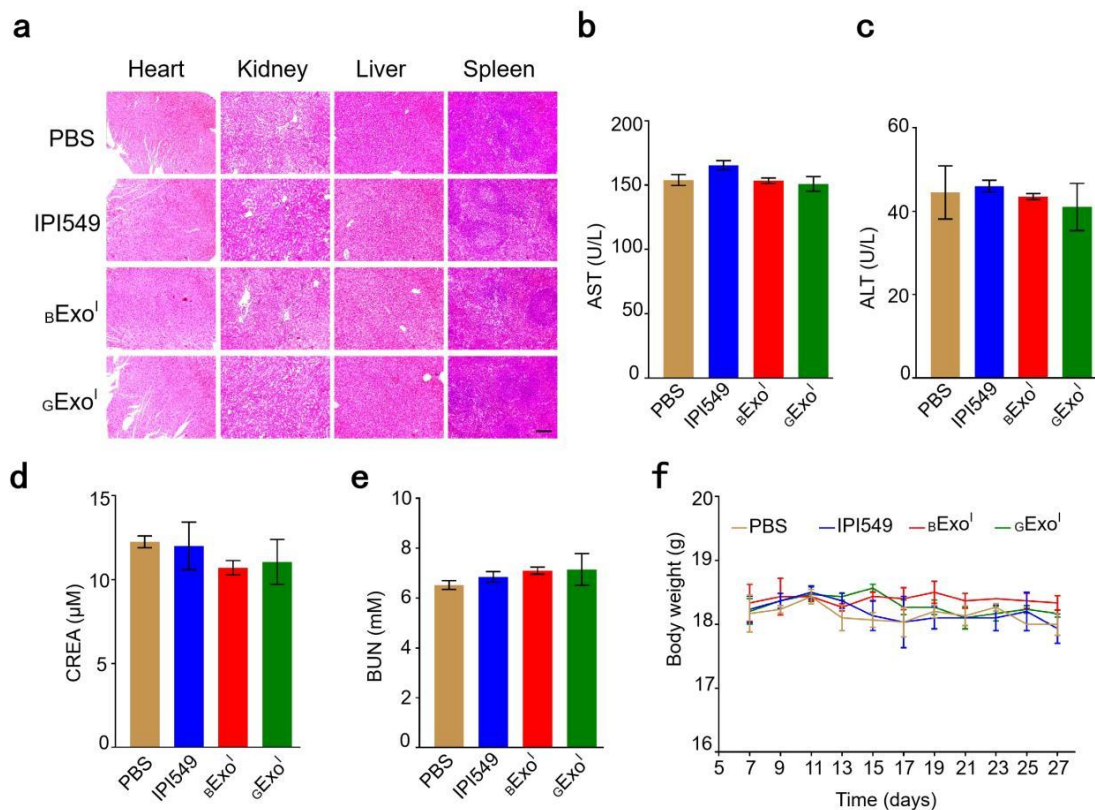
318
 319 **Figure 6. Prevented PMN formation by α Exo^l in the lung of postoperative lung metastasis mice. a**
 320 **Flow cytometry analysis of the percentage of G-MDSCs. b Western blot analysis of the PI3K γ**
 321 **expression in G-MDSCs. c Flow cytometry analysis of the percentages of mo-MDSCs and M2**
 322 **macrophages. d Flow cytometry analysis of the percentage of CD4⁺ T cells and CD8⁺ T cells. e, f**
 323 **ELISA analysis of the level of IFN γ e and IL10 f. For Figure 6a-f, mice whose subcutaneous tumors**
 324 **(100 mm³) were completely excised were intravenously injected with B16/F10 cells at 7 days**
 325 **post-surgery. PBS, free IPI549, β Exo^l and α Exo^l were injected intravenously to the mice every two days**
 326 **after injection with B16/F10 cells. All mice were sacrificed at 2 weeks after intravenous injection with**

327 B16F10 cells. And the lungs of the mice were used to prepare single-cell suspensions and lung
 328 homogenates for flow cytometry and ELISA analysis. Data are expressed as means \pm SD. n = 5
 329 biologically independent animals per group.

330

331 6. In vivo biocompatibility of α Exo^l

332 *In vivo* biocompatibility of α Exo^l was assessed by histological examination of major organs and
 333 blood chemistry tests. No noticeable damage was found in H&E stained tissue sections of major organs
 334 (heart, liver, spleen, lung and kidney) of mice at the end of treatments with IPI549, β Exo^l or α Exo^l (**Fig.**
 335 **7a**). Serum biochemical indices of aspartate aminotransferase (AST), alanine aminotransferase (ALT),
 336 creatinine (CREA) and blood urea nitrogen (BUN) in the mice treated with IPI549, β Exo^l or α Exo^l
 337 were not significantly different from those in the healthy mice (**Fig. 7b-e**), indicating that this
 338 therapeutic strategy may not cause obvious damage to the liver and spleen. Moreover, no body weight
 339 loss was found in all the mice groups during the treatment process in the postoperative lung metastasis
 340 mice model (**Fig. 7f**). Taken all together, α Exo^l is a biocompatible choice for the suppression of
 341 metastasis.



342

343 **Figure 7. In vivo biocompatibility of α Exo^l.** a H&E staining of major organ sections of mice treated

344 with IPI549, ${}_{\text{B}}\text{Exo}^{\text{I}}$ or ${}_{\text{G}}\text{Exo}^{\text{I}}$. Scale bar, 200 μm . **b-e** Levels of AST **b**, ALT **c**, CREA **d** and BUN **e** in
345 serum. **f** Mice body weight curves during the treatment period. Data are expressed as means \pm SD. n =
346 5 biologically independent animals per group.

347

348 Discussion

349 Functional exosomes (${}_{\text{G}}\text{Exo}^{\text{I}}$) were designed to suppress the lung metastasis of melanoma by
350 preventing the PMN formation. ${}_{\text{G}}\text{Exo}^{\text{I}}$ that presented GFE1 peptide on the surface of exosomal
351 membrane and loaded IPI549 inside the exosomes showed the significant targeting ability to
352 pulmonary vascular endothelial cells and inhibit G-MDSCs accumulation in the premetastatic lung. In
353 transwell system, ${}_{\text{G}}\text{Exo}^{\text{I}}$ targeting to MPVEC could release IPI549 to inhibit the migration of
354 G-MDSCs and decrease their PI3K γ expression. In postoperative mice model, intravenously injected
355 ${}_{\text{G}}\text{Exo}^{\text{I}}$ exhibited a significant aggregation effect in the lung PMN, and transformed immunosuppressive
356 microenvironment into immunostimulative microenvironment by decreasing the percentages of
357 G-MDSCs, mo-MDSCs and M2 macrophage and increasing the percentages of CD4 $^{+}$ T cells and CD8 $^{+}$
358 T cells, leading to the effective inhibition on tumor metastasis. Collectively, we provided herein a proof
359 of concept that early blocking the PMN formation using organ-specific exosomes would afford a potent
360 platform of anti-tumor organ specific metastasis.

361

362 Materials and methods

363 **1. Isolation of primary bone marrow MSCs.** Primary bone marrow MSCs were isolated from 2 or 3
364 week old C57BL/6 mice as previously described[39]. Briefly, bone marrow cells from the femur and
365 tibia were flushed thoroughly with a 26-gauge syringe needle inserted into the marrow cavity.
366 Afterwards, the diaphyses of femur and tibia were chopped into small sclerites and digested with
367 collagenase II for 2 h at 37°C in a shaker, 100 rpm min $^{-1}$. During digestion, bone marrow cells were
368 filtered using a 70 μm strainer filter and centrifuged at 200 g for 5 min. The cell pellet was resuspended
369 in C57BL/6 MSC complete culture medium (Cyagen Biosciences Inc, United States) and seeded in
370 culture dishes. After digestion, bone chips were washed 3 times with basic DMEM/F-12 and seeded

371 into the culture dishes to co-culture with the bone marrow cells at 37°C containing 5% CO₂. After
372 being seeded for 3 days, MSCs attached to the bottom of culture dishes and the non-adherent cells were
373 eliminated through the exchange of the cell medium at 72 hours and every 2 days thereafter. Then the
374 MSCs were identified by stained with anti-CD44-PE (clone IM7, Biolegend), anti-CD45-PE (clone
375 30-F11, Biolegend), anti-CD105-PE (clone MJ7/18, Biolegend), anti-CD34-PE (clone SA376A4,
376 Biolegend) and anti-CD29-FITC (clone HMβ1-1, Biolegend) by flow cytometry (BD Biosciences,
377 AccuriC6). The MSCs from passage 3 to passage 8 were implemented to extract exosomes.

378 **2. Preparation of ${}_G\text{Exo}^I$ and ${}_B\text{Exo}^I$.** The pEGFP-C1-GFE1-Lamp2b plasmid was constructed by the
379 Beijing Genomics institution (China). 1×10^7 MSCs were seeded into 100 mm dish. After 24 h, the
380 MSCs were transfected with 8 μg pEGFP-C1-GFE1-Lamp2b plasmid using Lipofectamine 2000
381 transfection reagent (Invitrogen, USA). After 24h transfection, the transfected MSCs were washed 3
382 times with PBS and cultured for another 24 h in media with exosome-free serum containing 40 $\mu\text{g mL}^{-1}$
383 IPI549. The exosomes were purified using a gradient centrifugation protocol according to the literature
384 [51]. The cell culture supernatant containing exosomes was harvested by centrifugation at 200 g for 5
385 min to eliminate cells. The supernatant was then centrifuged at 12,000 g for 45 min to remove dead
386 cells and cell debris. The resulting supernatant was further centrifuged at 100,000 g for 90 min
387 (QPTimaMAX-XP Ultra-High, Beckman Coulter, USA). The pellets were washed with large volume of
388 cold PBS and centrifuged at 120,000 g for 70 min again to ensure maximal exosome purity. All
389 centrifugation procedures were performed at 4 °C. The pellet of ${}_G\text{Exo}^I$ was resuspended in PBS and
390 stored at -80°C. ${}_B\text{Exo}^I$ was prepared using the similar procedure except using the pEGFP-Lamp2b
391 plasmid instead of the pEGFP-C1-GFE1-Lamp2b plasmid. ${}_G\text{Exo}$ and ${}_B\text{Exo}$ were prepared using the
392 similar preparation procedure of ${}_G\text{Exo}^I$ and ${}_B\text{Exo}^I$, respectively, except without IPI549 incubation.

393 **3. Characterization of exosomes.** The primary size and morphology of exosomes were examined
394 using transmission electron microscope (JEM-2010) and cryo-TEM (JEOL JEM-3200FSC).
395 Hydrodynamic size of purified exosomes was determined using Malvern Zetasizer (Nano ZS, Malvern,
396 USA). To confirm successful isolation of exosomes from MSCs, the presence of TSG101, CD63 and
397 CD9 on the exosome surface were measured by western blotting as mentioned by previous description
398 [52]. The primary antibodies were shown below: anti-CD9 (Abcam, UK), anti-CD63 (Abcam, UK),
399 anti-TSG101 (Abcam, UK). The amount of IPI549 loaded into exosomes was measured by a high
400 performance liquid chromatography (HPLC, Waters, USA) at 254 nm. 25 µg _BExo^I or _GExo^I in a 1.5
401 mL centrifuge tube was heated at 75 °C to evaporate solvent. Then, 100 µL of acetonitrile was added
402 and the mixture was vortexed, sonicated and then centrifuged at 12,000 rpm for 10 min. The
403 supernatant was collected and filtered through 0.22 µm microfiltration membrane. 20 µL of aliquots
404 was injected into the HPLC system. The chromatographic conditions were as follows: the column was
405 C18 column (4.6 × 250 mm, 5 µm); the mobile phase consisted of acetonitrile: 0.1% formic acid
406 (35:65); the column temperature was 25 °C and the detection wavelength was 254 nm [28, 53].

407 The loading capacity and encapsulation efficiency of IPI549 were calculated using the following
408 formula, where W₁ was the weight of the IPI549 enveloped in the _GExo^I, W was the weight of the
409 exosomes, and W₀ was the initial amount of IPI549 added to the culture medium.

$$LC\% = \frac{W_1}{W} \times 100\%$$

$$EE\% = \frac{W_1}{W_0} \times 100\%$$

410

411 **4. Release assessment of IPI549 from exosomes**

412 129.6 µg _BExo^I or 112.4 µg _GExo^I (containing 20 µg IPI549) suspended in 1 mL of PBS containing
413 0.5% carboxymethyl cellulose (CMC) and added to the dialysis bag with a 3500 molecular weight (Mw)

414 cutoff. Then, the dialysis bag was immersed in a flask containing 200 mL of PBS and 0.5% anionic
415 surfactant sodium dodecyl sulfate (SDS) at 37°C. Samples were taken at time points from inside the
416 flask, and the amount of released IPI549 was analyzed HPLC.

417 **5. Identification of GFE1 expression on exosomes.** 10 µg of His-tagged recombinant DPEP1
418 (Creative BioMart, USA) was incubated with 100 µg of $BExo^I$ or $GExo^I$ for 4 h at 4°C. Then $BExo^I$ or
419 $GExo^I$ was purified by ultracentrifugation. The expression of His-tag in $BExo^I$ and $GExo^I$ were analyzed
420 by western blot. The primary antibody was shown below: anti-6×His-tag (Abcam, UK)

421 **6. Exosome labeling.** The fluorescent dye, PKH26 (Umibio, China) was used to label exosomes.
422 Purified exosomes were incubated in 5 mM PKH26 for 15 min at 37°C, and then ultracentrifuged at
423 120,000 g for 90 min to remove free dye. After being washed twice in PBS, the PKH26-labeled
424 exosomes were resuspended in PBS prior to use.

425 **7. Cells culture.** B16/F10 and RAW 264.7 cells were purchased from the American Type Culture
426 Collection (ATCC). MPVEC and MLE12 were separated from the lung of mice. All cells were cultured
427 in Dulbecco's modified Eagle's medium (Gibco) supplemented with 10% heat-inactivated fetal bovine
428 serum (Gibco) and 1% penicillin/streptomycin, and maintained in 5% CO₂ at 37°C.

429 **8. Animals.**

430 Female C57BL/6J mice (4–6-weeks-old) were purchased from the Animal Experimental Center of Jilin
431 University (Changchun, China) and kept under thermo-regulated, humidity-controlled conditions under
432 a 12 h day/night light cycle provided by the experimental and were fed with standard rat chow and
433 water ad libitum. All animal studies were carried out in Changchun Institute of Applied Chemistry,
434 Chinese Academy of Sciences, the operating procedures of the experimental animals were carried out
435 in accordance with protocols approved by the Committee for Animal Research of Changchun Institute

436 of Applied Chemistry, Chinese Academy of Sciences China.

437 **9. Preparation of TCM.**

438 B16/F10 cells were cultured in DMEM with 10% FBS, 100 mg/mL streptomycin, and 100 U/mL
439 penicillin at 37 °C in a humidified atmosphere containing 5% CO₂. When the cells formed a
440 consecutive monolayer, the media was replaced with serum-free DMEM, and the cells were incubated
441 for 24 h. Then, the medium was collected and centrifuged. The supernatant was filtered through 0.22
442 μm syringe filters and stored at -20°C.

443 **10. Postoperative lung metastasis mouse model.** For *in vivo* metastasis model, B16/F10 cells ($1.0 \times$
444 10^6 cells) were subcutaneously injected at the back of C57BL/6 mice to establish the *in situ* melanoma
445 model. When the tumor size reached 100 mm³ (tumor volume = (length \times width²)/2), tumors were
446 surgically excised. Seven days later, mice were intravenously injected with B16/F10 cells (2.0×10^5
447 cells) and the postoperative pulmonary metastasis mouse model was established.

448 **11. Cytotoxicity assessment of exosomes.** RAW264.7 cells and HUVEC in logarithmic growth phase
449 were digested into single-cell suspensions and seeded in 96-well plates at 1×10^4 cells per well, and
450 then incubated in 5% CO₂ at 37°C overnight. Then, the medium was replaced with 100 μL of fresh
451 medium containing various concentrations of IPI549, _BExo^I or _GExo^I. After another 24 h of incubation,
452 10 μL of CCK-8 reagent (CCK8, Beyotime, Shanghai, China) was added to each well and then cultured
453 for 2 hours. The absorbance was measured at 450 nm by microplate reader (Bio-Rad, Hercules, CA,
454 USA) using wells without cells as blanks.

455 **12. In vitro Assessment of targeting ability of _GExo^I to MPVEC.** 1.5×10^5 MPVEC were incubated
456 with 100 μg mL⁻¹ PKH26-labeled _BExo^I or _GExo^I for 2 h. MLE12 cells used as control were similarly
457 treated. The cells were washed with PBS three times and visualized by fluorescence microscopy

458 (Nikon Eclipse 80i).

459 **13. G-MDSCs sorted from the blood and lung of tumor-bearing mice.**

460 To isolate G-MDSCs from blood, 2 week tumor-bearing mice were sacrificed by tail vein injection of
461 4% EDTA. Blood was collected, and the erythrocytes were eliminated with hypotonic lysis buffer. The
462 remaining cells were collected. To isolate G-MDSCs from lung, single cell suspensions of lungs were
463 prepared by cutting the organs into small fragments, digesting them at 37°C for 1 hour with 1 mg mL⁻¹
464 collagenase I and then filtering them through a 70 µm cell strainer. Erythrocytes were lysed with Red
465 Blood Cell Lysis Buffer (Beyotime, China). The G-MDSCs were sorted with a Myeloid-Derived
466 Suppressor Cell Isolation Kit using an AutoMACS sorter (Miltenyi Biotec, Germany) according to the
467 manufacturer's instructions. 1 × 10⁸ cells from blood or lungs were centrifuged at 300 g for 10 min at
468 4°C. The cell pellets were resuspended in 700 µL of PBS (pH 7.2), 0.5% bovine serum albumin, and 2
469 mM EDTA. Fetal bovine serum (50 µL) was added, mixed well, and incubated for 10 min at 4°C. After
470 incubation, 100 µL of biotin-conjugated anti-Ly6G antibody was added and the cells incubated for a
471 further 15 min at 4°C. Cells were washed by adding 10 mL of buffer and centrifuging at 300 g for 10
472 min at 4°C. The labeled cells were resuspended in 800 µL of buffer; then, 200 µL of anti-biotin
473 microbeads was added, mixed well, and incubated for 10 min at 4°C. Cells were washed by adding 10
474 mL of buffer and centrifuging at 300 g for 10 min at 4°C. The cell pellets were then resuspended in 500
475 µL of buffer. Then, the cell suspension was loaded onto a MACS column, which was placed in the
476 magnetic field of a MACS Separator. The magnetically labelled G-MDSCs cells were retained in the
477 column and washed from the column.

478 **14. The inhibition of α Exo^I on G-MDSCs chemotactic migration *in vitro*.** 5.0×10⁴ G-MDSCs sorted
479 from the blood of tumor-bearing mice were seeded onto transwell inserts with a polyethylene

480 terephthalate membrane pore size of 5 μm (Corning) in 24-well plates, while CXCL1 (10 ng mL⁻¹
481 PeproTech Co., Ltd., USA) was added into the lower chamber. Then, 50 $\mu\text{g mL}^{-1}$ _BExo, _GExo, _BExo^I or
482 _GExo^I were added to the upper chamber for 4 h. Then the number of G-MDSCs migrated into the lower
483 chamber was counted by flow cytometry (BD Biosciences, AccuriC6). To further evaluate the
484 inhibitory effect of _GExo^I targeting MPVEC on G-MDSC migration, MPVEC were first incubated with
485 100 $\mu\text{g mL}^{-1}$ _GExo^I or _BExo^I for 2 h, and then the cells were collected and washed with PBS for 3 times
486 to remove unbound exosomes. 1.0×10^5 G-MDSCs and 1.0×10^5 these exosome-treated MPVEC were
487 cultured in the upper chamber while CXCL1 (10 ng mL⁻¹) in the lower chamber for 4 h. Then the
488 number of G-MDSCs migrated into the lower chamber was counted by flow cytometry. The percentage
489 of migrated G-MDSCs = the number of migrated G-MDSCs/ the total number of G-MDSCs.

490 **15. Inhibitory effect of exosomes on PI3K γ expression in G-MDSCs.** G-MDSCs in the upper
491 chamber of transwell system were harvested or G-MDSCs in the lung of postoperative lung metastasis
492 mice treated with PBS, IPI549, _BExo^I or _GExo^I through intravenously injection were sorted. Then the
493 G-MDSCs were washed with PBS, and mixed with 50 μL cell lysate buffer (Beyotime, China).
494 Samples were centrifuged at 4 °C and 12,000 rpm, 30 min, and the supernatant was collected for
495 Western blot assay. The proteins of the collected supernatant were separated by sodium dodecyl
496 sulfate-polyacryl amide gel electrophoresis (SDS-PAGE) and transferred onto nitrocellulose blotting
497 membranes (GE Healthcare Life Science, Boston, Massachusetts). Anti-PI3K γ (1:1000, Santa Cruz
498 Biotechnology, USA) was incubated with the membrane overnight at 4°C. Horseradish
499 peroxidase-conjugated goat anti-mouse or goat anti-rabbit IgG secondary antibody (1:1000, Beyotime,
500 China) was incubated with the membranes for 1 h at room temperature. The proteins on the membranes
501 were detected using a Tanon imaging system (5200, Shanghai, China).

502 **16. Pharmacokinetics and distribution of exosomes.** The tissue distribution and bioavailability of
503 free IPI549, β Exo^I and γ Exo^I in mice were detected as following method [54]. Briefly, healthy C57BL/6
504 mice were randomly divided into three groups, namely, free IPI549, β Exo^I and γ Exo^I, weighed and
505 intravenously injected with a single dose of various formulations at 0.2 mg kg⁻¹ equivalent to the
506 content of IPI549. Blood samples were periodically collected via eye sinus bleeding and immediately
507 centrifuged to obtain plasma for determining IPI549 content at different time point by HPLC. At 24 h
508 after dosing, all the animals were euthanized and their tissues (liver, kidney, lung) were immediately
509 dissected out and homogenized to extract the IPI549 for HPLC analysis. To further monitor the
510 distribution of β Exo^I and γ Exo^I in mice, the C57BL/6 mice were randomly divided into three groups,
511 PBS, PKH26-labeled β Exo^I and PKH26-labeled γ Exo^I, weighed and intravenously administered a
512 single dose of various formulations at 0.2 mg/kg equivalent to the content of IPI549. After 24 h, the
513 hearts, livers, spleens, lung and kidneys of the mice were dissected, and a fluorescence imaging system
514 (Davinch-Invivo) was employed to capture the PKH26 fluorescence images of the organs.

515 **17. *In vivo* targeting ability assessment**

516 PKH26-labeled β Exo^I or γ Exo^I were intravenously injected into healthy C57BL/6 mice (0.2 mg of
517 IPI549-equiv per kg of body weight), and the treated mice were sacrificed after 24 h. Lung tissues were
518 collected and embedded in opti-mum cutting temperature compound (Sakura; Torrance, CA). The
519 frozen sections were fixed with acetone, incubated with 2 μ g mL⁻¹ anti-mouse CD31 antibody (Abcam,
520 UK) overnight at 4°C, and then stained with FITC rabbit anti-goat IgG (H+L) (1:500 dilution,
521 ABclonal) for 1 h at room temperature. The fluorescent signals of section were detected under
522 fluorescence microscopy.

523 **18. Metastasis prevention assay in TCM-stimulating mice model.** Tumor conditioned medium (200

524 μL) was intravenously injected into C57BL/6 mice one time per day for 3 days. After each TCM
525 injection on the same day, the mice were intravenously injected with IPI549, ${}_{\text{B}}\text{Exo}^{\text{I}}$ and ${}_{\text{G}}\text{Exo}^{\text{I}}$ (0.2 mg
526 kg^{-1} equivalent to the content of IP549). Then, B16/F10 cells (2.0×10^5 cells) were intravenously
527 injected after 3 days. The lungs were harvested after 14 days of B16/F10 cells intravenous injection and
528 the number of macroscopic metastatic nodules in the lung was recorded.

529 **19. *In vivo* efficacy of ${}_{\text{G}}\text{Exo}^{\text{I}}$ preventing PMN formation and against pulmonary metastases**

530 Female C57BL/6 mice with established postoperative lung metastasis were randomly divided into 4
531 groups: PBS, IPI549, ${}_{\text{B}}\text{Exo}^{\text{I}}$ and ${}_{\text{G}}\text{Exo}^{\text{I}}$ (0.2 mg kg^{-1} equivalent to the content of IP549). Each
532 intravenous injection was administered every other day (total for 6 doses) through the tail vein. The
533 first treatment was 2 days after the establishment of the postoperative lung metastasis model. Two days
534 after the last injection, animals were sacrificed to harvest lungs, and the number of macroscopic
535 metastatic nodules in each lung was recorded to evaluate the therapeutic effects. Furthermore, single
536 cell suspensions of a piece of the lungs were prepared as described above to detect the percentage of
537 G-MDSCs and mo-MDSCs through staining with anti-CD11b-FITC (clone M1/70, BD),
538 anti-CD45-PE/Cy7 (clone 30-F11, BD), anti-Ly6G-APC/Cy7 (clone 1A8, BD) and anti-Ly6C-PE
539 (clone AL-21, BD), respectively, to detect the percentage of $\text{CD4}^+\text{T}$ cells and $\text{CD8}^+\text{T}$ cells through
540 staining with anti-CD3-FITC (clone 17A2, Biolegend), anti-CD4-PE (clone GK1.5, Biolegend) and
541 anti-CD8-APC (clone 53-6.7, Biolegend), respectively, and to detect the percentage of M2 phenotype
542 macrophages through staining with anti-F4/80-FITC (clone BM8, Biolegend) and anti-CD206-APC
543 (clone C068C2, Biolegend), respectively, by flow cytometry (BD Biosciences, AccuriC6). A piece of
544 lung was homogenized to examine the level of $\text{IFN}\gamma$ and IL10 using Elisa kit (Biolegend, USA)
545 according to manufacturer's instruction. Afterwards, a piece of the lungs was fixed in 4%

546 paraformaldehyde, and then sliced into 5 μm -thick sections. Histological examinations of the lung
547 slices were performed with H&E staining for visualization of metastatic foci.

548 **20. Toxicity Evaluation in Vivo.**

549 The body weight of each mouse was measured every 2 day from tumors excised. At the end of
550 systematic administration, major organs (heart, liver, spleen, and kidney) were harvested as mentioned
551 above and served for H&E staining and aspartate transaminase (AST), alanine transaminase (ALT),
552 creatinine (CREA) and blood urea nitrogen (BUN) levels of serum collecting from different treated
553 mice were detected using a commercial kit (Nanjing Institute of Biological Engineering, Nanjing,
554 China) according to the manufacturer's protocol.

555 **21. Statistical analysis.** All data analyses were performed using GraphPad Prism 6.0 (GraphPad
556 Software, La Jolla, CA, USA). Data are presented as the mean \pm SD. Student's t-test was used to
557 analyze differences between two groups. One-way ANOVA was used to perform the multi-sample
558 analysis followed by the Tukey post hoc test. Differences at $P < 0.05$ were considered statistically
559 significant .

560

561 Author contributions

562 Conceptualization, methodology, investigation: Xiaoqing Han; investigation, manuscript revision:
563 Luopeng Bi; investigation, methodology, formal analysis: Yunyun Wu, Jiao Yan, Xiaoqing Wu, Runxiao
564 Zheng, Yingying Sun and Yanbo Wang; conceptualization, writing-review & editing, manuscript
565 revision, supervision, visualization: Haiyuan Zhang

566

567 Conflicts of interest

568 The authors declare no competing financial interest.

569

570 Acknowledgements

571 This work was primarily supported by the National Natural Science Foundation of China (22007087

572 and 22077119).

573

574 References

575 1. Bray, F., et al. Global cancer statistics 2018: GLOBOCAN estimates of incidence and mortality
576 worldwide for 36 cancers in 185 countries. *CA. Cancer J Clin.* **68**, 394-424 (2018).

577 2. Fidler, I.J. The pathogenesis of cancer metastasis: the 'seed and soil' hypothesis revisited. *Nature*
578 *Reviews Cancer.* **3**, 453-458 (2003).

579 3. Wan, L., K. Pantel, & Kang, Y. Tumor metastasis: moving new biological insights into the clinic. *Nat.*
580 *Med.* **19**, 1450-1464 (2013).

581 4. Chambers, A.F., Groom, A.C. & MacDonald, I.C. Dissemination and growth of cancer cells in
582 metastatic sites. *Nat. Rev. Cancer.* **2**, 563-572 (2002).

583 5. Steeg, P.S. Targeting metastasis. *Nat. Rev. Cancer.* **16**, 201-218 (2016).

584 6. Ganesh, K. & Massague, J. Targeting metastatic cancer. *Nat. Med.* **27**, 34-44 (2021).

585 7. Li, W., Yu Y., Wang, H., Yan, A. & Jiang, X. Evaluation of the prognostic impact of postoperative
586 adjuvant radiotherapy on head and neck mucosal melanoma: a meta-analysis. *BMC. Cancer.* **15**, 758
587 (2015).

588 8. Langley, R.R. & Fidler, I.J. Tumor cell-organ microenvironment interactions in the pathogenesis of
589 cancer metastasis. *Endocr. Rev.* **28**, 297-321 (2007).

590 9. Kaplan, R.N., et al. VEGFR1-positive haematopoietic bone marrow progenitors initiate the
591 pre-metastatic niche. *Nature.* **438**, 820-827 (2005).

592 10. Liu, Y. & Cao, X. Characteristics and Significance of the Pre-metastatic Niche. *Cancer Cell.* **30**,
593 668-681 (2016).

594 11. Quail, D.F. & Joyce, J.A. Microenvironmental regulation of tumor progression and metastasis.
595 *Nature Medicine.* **19**, 1423-1437 (2013).

- 596 12. Sceneay, J., Smyth, M.J. & Möller, A. The pre-metastatic niche: finding common ground. *Cancer*
597 *and Metastasis Reviews*. **32**, 449-464 (2013).
- 598 13. Peinado, H., et al. Pre-metastatic niches: organ-specific homes for metastases. *Nat. Rev. Cancer*. **17**,
599 302-317 (2017).
- 600 14. Jiang, T., et al. Metformin and Docosahexaenoic Acid Hybrid Micelles for Premetastatic Niche
601 Modulation and Tumor Metastasis Suppression. *Nano Lett.* **19**, 3548-3562 (2019).
- 602 15. Long, Y., et al. Self-Delivery Micellar Nanoparticles Prevent Premetastatic Niche Formation by
603 Interfering with the Early Recruitment and Vascular Destruction of Granulocytic Myeloid-Derived
604 Suppressor Cells. *Nano Lett.* **20**, 2219-2229 (2020).
- 605 16. Sceneay, J., et al. Primary tumor hypoxia recruits CD11b⁺/Ly6C^{med}/Ly6G⁺ immune suppressor
606 cells and compromises NK cell cytotoxicity in the premetastatic niche. *Cancer Res.* **72**, 3906-3911
607 (2012).
- 608 17. Wang, Y., Ding, Y., Guo, N., & Wang, S., et al., MDSCs: Key Criminals of Tumor Pre-metastatic
609 Niche Formation. *Front Immunol.* **10**, 172-188 (2019).
- 610 18. Kowanzet, M., et al. Granulocyte-colony stimulating factor promotes lung metastasis through
611 mobilization of Ly6G⁺Ly6C⁺ granulocytes. *Proc. Natl. Acad. Sci. USA.* **107**, 21248-21255 (2010).
- 612 19. Kitamura, T., Qian, B.-Z. & Pollard, J.W. Immune cell promotion of metastasis. *Nat. Rev. Immunol.*
613 **15**, 73-86 (2015).
- 614 20. Engblom, C., Pflirschke, C. & Pittet, M.J. The role of myeloid cells in cancer therapies. *Nat. Rev.*
615 *Cancer*. **16**, 447-462 (2016).
- 616 21. Yan, H.H., et al. Gr-1⁺CD11b⁺ myeloid cells tip the balance of immune protection to tumor
617 promotion in the premetastatic lung. *Cancer Res.* **70**, 6139-6149 (2010).
- 618 22. Ouzounova, M., et al. Monocytic and granulocytic myeloid derived suppressor cells differentially
619 regulate spatiotemporal tumour plasticity during metastatic cascade. *Nat. Commun.* **8**, 14979-14992
620 (2017).
- 621 23. Kumar, V., Patel, S., Tcyganov, E. & Gabrilovich, D. The Nature of Myeloid-Derived Suppressor
622 Cells in the Tumor Microenvironment. *Trends Immunol.* **37**, 208-220 (2016).
- 623 24. Zhou, Y. & Guo, F. A selective sphingosine-1-phosphate receptor 1 agonist SEW-2871 aggravates
624 gastric cancer by recruiting myeloid-derived suppressor cells. *J. Biochem.* **163**, 77-83 (2018).
- 625 25. Cheng, Y., et al. Potential roles and targeted therapy of the CXCLs/CXCR2 axis in cancer and

626 inflammatory diseases. *Biochim. Biophys. Acta Rev. Cancer.* **1871**, 289-312 (2019).

627 26. Wang, D., Sun, H., Wei, J., Cen, B., & DuBois, R. CXCL1 Is Critical for Premetastatic Niche
628 Formation and Metastasis in Colorectal Cancer. *Cancer Res.* **77**, 3655-3665 (2017).

629 27. Ferguson, G.J., et al. PI(3)Kgamma has an important context-dependent role in neutrophil
630 chemokinesis. *Nat. Cell Biol.* **9**, 86-91 (2007).

631 28. Gao, Y., et al. Metastasis Organotropism: Redefining the Congenial Soil. *Dev. Cell.* **49**, 375-391
632 (2019).

633 29. Creasy, J.M., et al. Actual 10-year survival after hepatic resection of colorectal liver metastases:
634 what factors preclude cure? *Surgery.* **163**, 1238-1244 (2018).

635 30. Parker, C., et al. Alpha emitter radium-223 and survival in metastatic prostate cancer. *N. Engl. J.*
636 *Med.* **369**, 213-223 (2013).

637 31. Pegtel, D.M. & Gould, S.J. Exosomes. *Annu. Rev. Biochem.* **88**, 487-514 (2019).

638 32. Tian, Y., et al. A doxorubicin delivery platform using engineered natural membrane vesicle
639 exosomes for targeted tumor therapy. *Biomaterials.* **35**, 2383-2390 (2014).

640 33. Tian, R., et al. Tumor Exosome Mimicking Nanoparticles for Tumor Combinatorial
641 Chemo-Photothermal Therapy. *Front Bioeng Biotechnol.* **8**, 1010-1021 (2020).

642 34. Bunggulawa, E.J., et al., Recent advancements in the use of exosomes as drug delivery systems. *J.*
643 *Nanobiotechnology.* **16**, 81-81 (2018).

644 35. Xiong, F., et al. Pursuing Specific Chemotherapy of Orthotopic Breast Cancer with Lung
645 Metastasis from Docking Nanoparticles Driven by Bioinspired Exosomes. *Nano Lett.* **19**, 3256-3266
646 (2019).

647 36. Zhao, L., et al. Exosome-mediated siRNA delivery to suppress postoperative breast cancer
648 metastasis. *J. Control Release.* **318**, 1-15 (2020).

649 37. Lv, Q., et al. Thermosensitive Exosome-Liposome Hybrid Nanoparticle-Mediated
650 Chemoimmunotherapy for Improved Treatment of Metastatic Peritoneal Cancer. *Adv. Sci (Weinh).* **7**,
651 2000515 (2020).

652 38. Alvarez-Erviti, L., et al. Delivery of siRNA to the mouse brain by systemic injection of targeted
653 exosomes. *Nat. Biotechnol.* **29**, 341-345 (2011).

654 39. Wang, X., et al. Engineered Exosomes With Ischemic Myocardium-Targeting Peptide for Targeted
655 Therapy in Myocardial Infarction. *J. Am. Heart Assoc.* **7**, e008737 (2018).

656 40. Zhuang, M., et al. SPION decorated exosome delivery of TNF-alpha to cancer cell membranes
657 through magnetism. *Nanoscale*. **12**, 173-188 (2020).

658 41. Smyth, T., et al. Surface functionalization of exosomes using click chemistry. *Bioconjug Chem*. **25**,
659 1777-1784 (2014).

660 42. Yeo, R.W., et al. Mesenchymal stem cell: an efficient mass producer of exosomes for drug delivery.
661 *Adv. Drug Deliv. Rev.* **65**, 336-341 (2013).

662 43. Rajotte, D. & Ruoslahti, E. Membrane dipeptidase is the receptor for a lung-targeting peptide
663 identified by in vivo phage display. *J. Biol. Chem.* **274**, 11593-11598 (1999).

664 44. Rajotte, D., et al. Molecular heterogeneity of the vascular endothelium revealed by in vivo phage
665 display. *J. Clin. Invest.* **102**, 430-437 (1998).

666 45. Wu, C.F., et al. The lack of type I interferon induces neutrophil-mediated pre-metastatic niche
667 formation in the mouse lung. *Int. J. Cancer.* **137**, 837-847 (2015).

668 46. Highfill, S.L., et al. Disruption of CXCR2-Mediated MDSC Tumor Trafficking Enhances Anti-PD1
669 Efficacy. *Sci. Transl. Med.* **6**, 237ra67 (2014).

670 47. Shi, H., et al. Chemokine (C-X-C motif) ligand 1 and CXCL2 produced by tumor promote the
671 generation of monocytic myeloid-derived suppressor cells. *Cancer Sci.* **109**, 3826-3839 (2018).

672 48. Sinha, P., Clements, V., Bunt, S., Albelda, S. & Ostrand-Rosenberg, S. Cross-Talk between
673 Myeloid-Derived Suppressor Cells and Macrophages Subverts Tumor Immunity toward a Type 2
674 Response. *J. Immunol.* **179**, 977-983 (2007).

675 49. Kak, G., M. Raza, & Tiwari, B.K. Interferon-gamma (IFN-gamma): Exploring its implications in
676 infectious diseases. *Biomol Concepts*. **9**, 64-79 (2018).

677 50. Hamidullah, Changkija, B. & Konwar, R. Role of interleukin-10 in breast cancer. *Breast Cancer Res.*
678 *Treat.* **133**, 11-21 (2012).

679 51. Yuan, D., et al. Macrophage exosomes as natural nanocarriers for protein delivery to inflamed brain.
680 *Biomaterials*. **142**, 1-12 (2017).

681 52. Su, D., et al. Exosomal PD-L1 functions as an immunosuppressant to promote wound healing. *J.*
682 *Extracell. Vesicles*. **9**, 1709262-1709262 (2019).

683 53. Zhang, X., Shen, L., Liu, Q., Hou, L. & Huang, L. Inhibiting PI3 kinase-gamma in both myeloid
684 and plasma cells remodels the suppressive tumor microenvironment in desmoplastic tumors. *J. Control*
685 *Release*. **309**, 173-180 (2019).

686 54. Wang, H., et al. Curcumin-primed exosomes potently ameliorate cognitive function in AD mice by
687 inhibiting hyperphosphorylation of the Tau protein through the AKT/GSK-3beta pathway. *Nanoscale*.
688 **11**, 7481-7496 (2019).

Supplementary Files

This is a list of supplementary files associated with this preprint. Click to download.

- [supplementaryinformation.pdf](#)